Geotextiles and Geomembranes 46 (2018) 497–510

Contents lists available at ScienceDirect

Geotextiles and Geomembranes

journal homepage: www.elsevier.com/locate/geotexmem

Energy efficiency of fibre reinforced soil formation at small element scale: Laboratory and numerical investigation

Erdin Ibraim[a,*], Jean-Francois Camenen[b,c], Andrea Diambra[a], Karolis Kairelis[d], Laura Visockaite[a], Nilo Cesar Consoli[e]

[a] Dept. of Civil Engineering, University of Bristol, UK
[b] University Bretagne Sud, FRE CNRS 3744, IRDL, F-56100 Lorient, France
[c] Formerly University of Bristol, UK
[d] Vattenfall UK, Formerly University of Bristol, UK
[e] Dept. of Civil Engineering, Federal University of Rio Grande do Sul, Av. Osvaldo Aranha, 99, Office 311H, Porto Alegre, 90035-190, Brazil

ARTICLE INFO

Keywords:
Geosynthetics
Soil reinforcement
Granular soil
Fibre
Compaction
Laboratory
Discrete element modelling

ABSTRACT

This paper explores the aspects related to the energy consumption for the compaction of unreinforced and fibre reinforced samples fabricated in the laboratory. It is well known that, for a fixed soil density, the addition of fibres invariably results in an increased resistance to compaction. However, similar peak strength properties of a dense unreinforced sample can be obtained using looser granular soil matrices mixed with small quantities of fibres. Based on both experimental and discrete element modelling (DEM) procedures, this paper demonstrates that less compaction energy is required for building loose fibre reinforced sand samples than for denser unreinforced sand samples while both samples show similar peak strength properties. Beyond corroborating the macro-scale experimental observations, the result of the DEM analyses provides an insight into the local micro-scale mechanisms governing the fibre-grain interaction. These assessments focus on the evolution of the void ratio distribution, re-arrangement of soil particles, mobilisation of stresses in the fibres, and the evolution of the fibre orientation distribution during the stages of compaction.

1. Introduction

Laboratory characterisation of the behaviour of fibre reinforced sand requires fabrication of small scale samples for element testing. The sample fabrication invariably includes a succession of several stages like soil-fibre mixing, deposition and compaction. Application of the use of short flexible and discrete fibres for the construction of real scale geotechnical systems will equally include mixing, deposition and compaction, but the procedure will certainly be more challenging due to the large volumes of material involved.

Mixing sand and fibres for laboratory element testing purposes is not a complex process, nor does it require highly technical skills. The amount of sand is relatively small and so is the fibre content, normally up to 1% by mass of dry soil. Fibres are added progressively to the sand which is in a moist condition and all the mixture is manually blended with the help of a little spoon until by visual inspection the operator is satisfied that the composite presents a uniform appearance. The formation of fibre reinforced sand samples commonly used in laboratory studies follows the so called moist tamping fabrication technique (Ladd, 1978). Although subjected to some criticism (Vaid et al., 1999; Eliadorani and Vaid, 2003; Frost and Park, 2003), this fabrication method, in the case of fibre reinforced sands, has the main advantage of preventing the segregation of fibres, while eventually producing a soil-fibre fabric which may resemble that of man-made compacted reinforced soils in the field.

The question of whether this soil-reinforcement technique aimed at increasing the strength and stability of sandy soils is reasonably more cost-effective than other methods that are currently being used in practice (for example, densification of granular soils by compaction) has never been investigated. As an initial attempt to assess the cost-effectiveness of the fibre reinforcement technique, this paper seeks to provide a fundamental analysis and quantitative estimation of the energy required for the compaction phase of samples formed in laboratory. A numerical assessment of the sample formation process based on Discrete Element Modelling (DEM) is also conducted to provide insight into the interaction mechanisms at the fibre and grain scale.

* Corresponding author.
E-mail addresses: erdin.ibraim@bristol.ac.uk (E. Ibraim), jfcamenen@gmail.com (J.-F. Camenen), andrea.diambra@bristol.ac.uk (A. Diambra), karolis.kairelis@vattenfall.com (K. Kairelis), laura_vis@yahoo.com (L. Visockaite), consoli@ufrgs.br (N.C. Consoli).

https://doi.org/10.1016/j.geotexmem.2018.04.008
Received 31 July 2017; Received in revised form 20 March 2018; Accepted 3 April 2018
Available online 25 April 2018

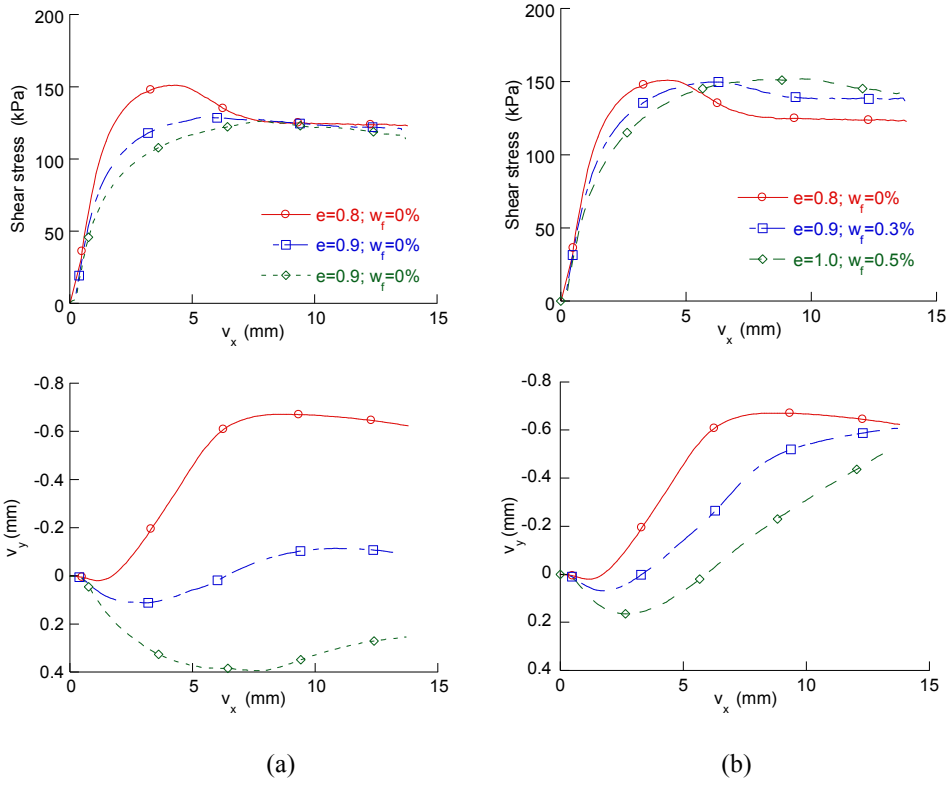

Fig. 1. Direct shear test results: (a) unreinforced samples and (b) one unreinforced and two reinforced samples.

2. Motivation

Standard laboratory compaction tests on fibre-reinforced sands indicate that fibre reinforcement provides resistance to compaction causing, for a given compaction energy, a less dense packing compared with unreinforced sand (Hoare, 1979; Murray et al., 2000; Ibraim and Fourmont, 2007). The maximum dry density of the reinforced sand also decreases with increasing fibre content. Although these observations may question the ability of the fibre-reinforcement technique to provide a cost-effective alternative to soil densification if, for example, the matrix density of the reinforced soil is to be preserved, the design process of fibre-reinforced soils may consider alternative approaches, such as using less sand material (loose state) reinforced with fibres that would provide strength properties like that of an unreinforced dense sand. Therefore, the assessment of cost-effectiveness should focus on the comparison between the compaction energy required for the formation of dense unreinforced sand and the compaction energy for the formation of less dense fibre-reinforced soils, providing that the mechanical characteristics of the latter are better than or at least similar to the former.

Fig. 1a shows the direct shear test results of three unreinforced sand samples (Hostun RF sand, Flavigny et al., 1990) of three void ratios, e (ratio between volume of voids and volume of solids) of 0.83, 0.94, 1.01 sheared under a normal stress of 208.5 kPa (Ibraim and Fourmont, 2007). Fig. 1a presents the variation of both the shear stress and vertical displacement (v_y) with the horizontal displacement (v_x) and reveals typical responses for a medium-dense, loose and very loose sand material. Fig. 1b shows similar direct shear test responses, but this time the loose and very loose sand samples are reinforced with polypropylene fibres (Loksand™) 0.3% and 0.5% fibre contents (w_f) by mass of dry sand, respectively. While the volumetric responses of the samples presented in Fig. 1b reflect the differences in the sample densities, with higher dilation for the dense unreinforced sample, the particularity here is that all samples present a similar peak shear stress response, around 150 kPa. If the densification process of the unreinforced medium-dense sand sample requires compaction energy, how does this compaction energy compare with the energy required to construct the fibre reinforced samples? An experimental procedure was devised to assess the compaction energy for these unreinforced and fibre-reinforced sample types. Parallel DEM simulations of analogue systems were equally conducted.

3. Experimental set up

The moist tamping fabrication method consists of compacting a wet soil by applying a monotonic load to successive layers of pre-definite height in a rigid mould using a light tamper (Ladd, 1978). The area of the tamper represents a fraction of the total cross-sectional area of the sample and, therefore, the compaction of a layer involves sequential horizontal re-positioning of the tamper once the soil underneath is vertically compressed. The tamper is attached to a rod and the verticality of the rod is assured by a guiding linear bearing system rigidly attached to a horizontal plate. The plate could be either supported by the sample's mould or by any other external prop, which in our set up consists of a transparent plexi-cylinder as shown in Fig. 3a. The compaction process does not use any mechanical loading system other than that provided by the human force. While the density of the sample is initially fixed, its control is performed by choosing the right amount of dry soil required for each successive layer and by ensuring that the soil is fully compacted within the desired layer volume.

The assessment of the compaction energy employed for the formation of each layer and for the whole sample requires the measurement of both compaction forces applied in each tamping effort and the corresponding vertical travel of the tamper. While the former measurement is provided by a load cell located between the tamping rod and the tamper, which eliminates the effects of parasitic rod friction of the rod/guiding bearing system, the latter is measured using a Linear Variable Differential Transformers (LVDTs) sensor attached to the reference collar as shown in Fig. 2a. The maximum capacity of the load cell is 5 kN and the measurement range of the LVDT is ± 20 mm. A

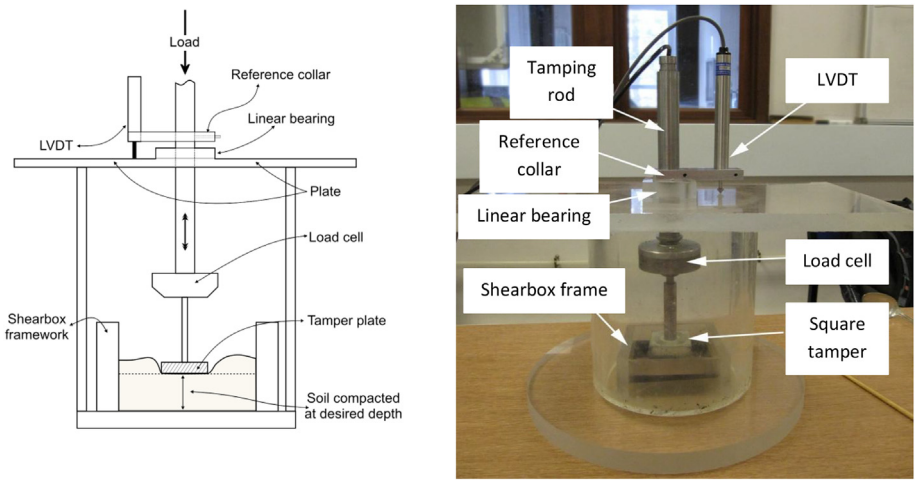

Fig. 2. (a) Schematic and (b) general view of the tamping system.

general picture of the experimental set up system is shown in Fig. 2b.

The fabrication of the unreinforced sample (ES08F0) and reinforced samples (ES09F03 and ES10F05) followed the same operations as those employed for the fabrication of the samples tested in the direct shear box by Ibraim and Fourmont (2007) and shown in Fig. 1b. In the name of the samples, ES designates 'Experimental Sample', 08, 09 and 10 indicate target void ratios of 0.8, 0.9 and 1.0 respectively, while F0, F03 and F05 label the amount of fibres, w_f, of 0%, 0.3% and 0.5% (by dry mass of sand), respectively. The same sand, Hostun RF, and same fibre type, Loksand™, have been used. Hostun RF is a standard European material for laboratory testing), has a silica content $SiO_2 > 98\%$ (Flavigny et al., 1990), and the particle shape is angular to sub-angular. The sand characteristics are listed in Table 1. Locksand™ are flexible polypropylene crimped fibres (Diambra et al., 2010, 2011; Ibraim et al., 2010; Diambra and Ibraim, 2014), their characteristics are also given in Table 1. The void ratio refers only to intergranular void ratio; the fibres, air and water are considered parts of the voids. For each generic sample density, seven identical samples have been fabricated and their averages of various compaction parameters were used for comparison purposes. As in the original direct shear experimental set up, all the samples have been fabricated in the same direct shear box with a volume of $100 \times 100 \times 45\,mm^3$. The sand/fibre mixing stage for all samples used approximately 10% of water by dry mass of sand. The sample formation included three layers of different heights, from bottom to top: 7.7 mm, 20 mm and 11.5 mm for unreinforced medium dense soil and 7.7 mm, 20 mm and 10 mm for fibre reinforced loose and very loose samples. For a typical layer, the corresponding amount of soil (with or without fibres) was carefully deposited into the box to ensure a zero-drop height and subsequently compacted to the target density using the tamping set up described above. The horizontal print area of the compaction square tamper plate was $50 \times 50\,mm^2$.

Table 1
Material characteristics in experiment and DEM.

Material characteristics	Experiment	DEM
Sand mean grain size, D_{50} (mm)	0.32	3.2
Coefficient of uniformity, $C_u = D_{60}/D_{10}C_u$	1.62	1.22
Coefficient of gradation, $C_g = (D_{30})^2/(D_{60}\,D_{10})$	1.0	1.0
Sand specific gravity, G_s	2.65	2.65
Fibre length, l_f (mm)	3.5	35
Fibre diameter, d_f (mm)	0.1	1.0
Fibre specific gravity, G_f	0.91	0.91

4. Numerical model

Insight into the mechanics of the 3D tamping sample formation has been gained through the Non-Smooth Contact Dynamic (NSCD) method (Jean and Moreau, 1992; Moreau, 1994). This model is a discrete element method (DEM) which simulates multi-bodies with multi-contacts

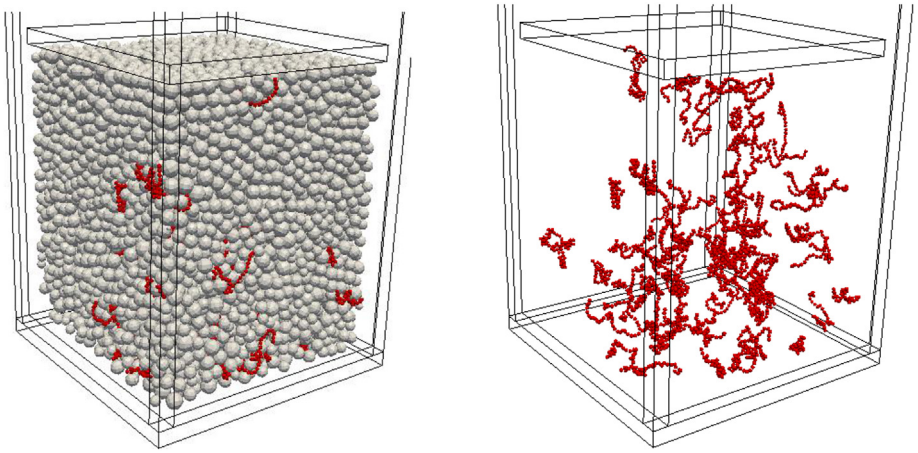

Fig. 3. Views of a 3D DEM numerically formed sample: first layer (left) and the fibre network (right).

interactions. The Non Smooth Contact Dynamics (NSCD) is based on implicit time integration approach, non-smooth formulation of mutual exclusion between particles and dry particle contact friction (Dubois and Jean, 2003; Cambou et al., 2010). The method is implemented in the LMGC90 software (Dubois and Jean, 2003). The granular material is modelled by rigid spheres the interaction of which is modelled by shock law. The algorithm solves the equations of motion of the rigid particles interacting through unilateral contacts. The normal and frictional interparticle forces are jointly implemented in NSCD as in Camenen et al. (2012), Camenen et al. (2013) and Camenen and Descantes (2017) with normal and tangential restitution coefficients as well as sliding friction coefficient. At each time step, both the kinematic constraints of all particles in the system and the equations of motion are simultaneously considered to determine the particle velocities and contact forces. An iterative process using a non-linear Gauss-Seidel like method is employed.

The granular matrix in the DEM simulations replicates approximately the particle size distribution of the Hostun RF sand used in the experimental investigation (see Table 1) but with the mean particle size multiplied by 10 to conveniently reduce the number of particles in the numerical calculations. A scale of 10 was also adopted for the modelling of the fibre dimensions (as shown in Table 1) to respect the experimental fibre to grain size ratio which has a major influence on the fibre-soil interaction (e.g. Gray and Ohashi, 1983; Diambra and Ibraim, 2015; Muir Wood et al., 2016). The fibres are flexible and were modelled as a collection of equidistant rigid spheres (specific gravity of 0.91) connected by unilateral wire elements as previously used for the modelling of flexible fibres and implemented in LMGC90 code by Laniel et al. (2008). For a pair of fibre particles, the wire contact law refers to the normal direction at the particle contact and only contact forces are transmitted, the effect being similar as a hinge connection type as proposed by Ibraim et al. (2006) and Maeda and Ibraim (2008). The tensile strength of the rigid wire was chosen based on tensile tests on real fibres conducted by Diambra et al. (2010) and this value (Table 2) showed to be sufficiently high to avoid fibre breakages (no fibre breakages were detected in the experiments either).

The mixing of real granular soil and fibres takes place in wet conditions as explained in the experimental investigation. The amount of water, 10% by mass of dry granular material, therefore creates inter-particle water menisci inducing particle bonds from capillary effects. The attractive capillary forces are introduced for all the particles in contact according to a pendular regime of distributed menisci (Mitarai and Nori, 2006). For the range of the particle sizes employed in this study, a single capillary force, F_c, which follows a square fit law is introduced as previously proposed by Saint-Cyr et al. (2013). The capillary force is fully active over a limit distance, d_c, between the surfaces of the particles joined by the liquid meniscus and becomes negligible beyond this limit. The total inter-particle normal force, R_N, combines the mutual exclusion force, F_N, and the capillary force, F_c. This law was successfully tested and implemented in NSCD by Saint-Cyr et al. (2013), while the values of d_c and F_c were assessed according to the relationships defined by Soulié et al. (2006) in a study related to cohesion in sand media. The input parameters for the 3D DEM simulations are listed in Table 2. The inter-particle friction coefficient was selected based on published work by Rowe (1962), Horn and Deere (1962), Cavarretta et al. (2011) and Senetakis et al. (2013). The values of the steel wall-particle and particle-fibre frictional coefficients are based on Lings and Dietz (2005) and Michalowski and Čermák (2003). The interaction between the wall and the fibres is very limited and in the absence of some experimental evidence, the wall-fibre friction coefficient was chosen similar as the particle-fibre friction coefficient.

Five granular samples, three unreinforced at void ratios of 0.8, 0.9 and 1.0 and two fibre reinforced, one with a 0.3% of fibre content (by dry weight of analogue granular material) and 0.9 intergranular void ratio and one with 0.5% fibre content and 1.0 intergranular void ratio were numerically generated and analysed. Each sample was formed under zero gravity conditions in a rigid mould of $64 \times 64\,mm^2$ square area base and comprised three layers of 77 mm (bottom), 200 mm (middle) and 100 mm (top) thickness. A factor of 10 exists between the height of the layers in the experiments and DEM simulations, while a reduced sample cross-sectional area in the numerical model was still considered representative with a characteristic size around twenty times the average grain size. The formation of each numerical fibre reinforced sample was designed to mimic as closely as possible the experimental procedure described above. For each layer, the fabrication firstly involved the generation of individual fibres by following a numerical protocol inspired by Laniel et al. (2008) and ensuring a random fibre orientation distribution. Once the fibres were generated, the analogue sand particles were placed in the container following a geometrical deposition algorithm developed by Taboada et al. (2005). At this stage, the sample is only geometrically admissible: there is no actual contact between particles and the sample is loose. In the next phase of sample formation, all the material was numerically compacted in a volume twice the target layer volume under zero gravity. The size of this volume was suggested by the experimental observations which showed that the deposited material in the mould occupied a volume approximately twice the target volume layer. Once this numerical protocol finalised, the physical compaction of the soil was conducted following five incremental compaction stages in a velocity-controlled mode with a constant speed of 0.2 m/s first by using a horizontal rigid tamper of $32 \times 32\,mm^2$ print area and then by employing a larger tamper which covered the entire cross-section of the sample. The small area tamper was applied four times in such a way that each time it covered one quarter of the horizontal section. After each incremental compaction stage, the final particle velocities were set to zero, while the tamper was horizontally repositioned but at the same initial level. A summary of the numerical samples including their names (NS designates a 'numerical sample'), fabrication conditions, number of particles and fibres is given in Table 3. Fig. 3a presents the appearance of the first layer for the sample NS09F03 at the end of the tamping process, while Fig. 3b isolates the fibre network (red spheres).

Table 2
Input parameters for the 3D discrete element method (DEM) simulations.

Input parameter	Value
Inter-particle friction coefficient	0.36
Wall-particle friction coefficient	0.36
Particle-fibre friction coefficient	0.34
Wall-fibre friction coefficient	0.34
Fibre normal particle contact strength	2×10^8 Pa
Capillary force, Fc	8×10^{-4} N
Limit distance between particles of capillary force action, d_c	0.5 mm
Normal restitution coefficient	0
Tangential restitution coefficient	0

5. Macro-scale observations

5.1. Compaction forces

The time sequence of the forces and the corresponding vertical

Table 3
List of numerical samples generated in this study.

Test name	Void ratio, e	Fibre content, w_f (%)	Number of granular particles	Number of fibres
NS08F0	0.8	0	49 500	0
NS09F0	0.9	0	45 700	0
NS10F0	1.0	0	42 700	0
NS09F03	0.9	0.3	45 700	398
NS10F05	1.0	0.5	42 700	624

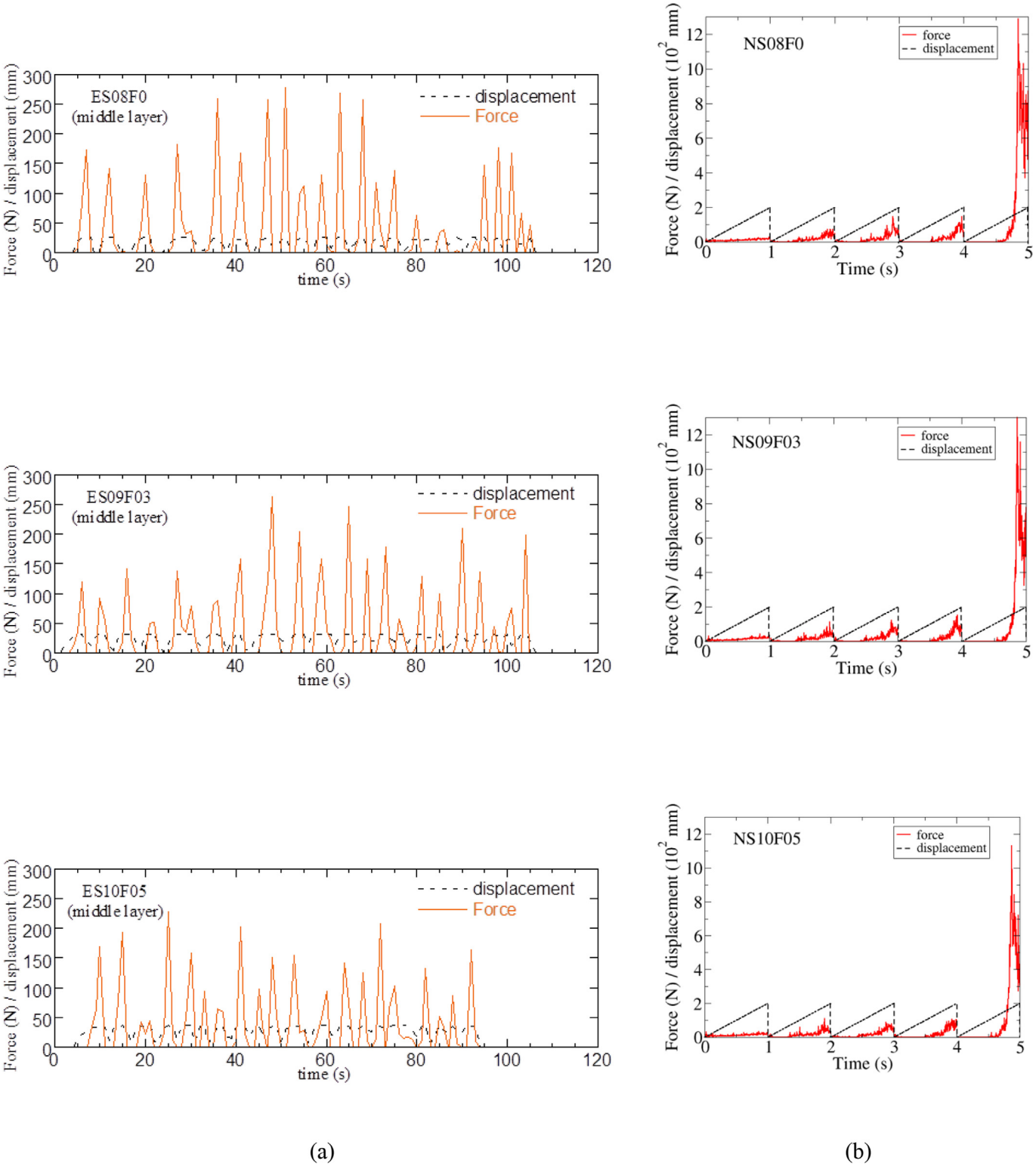

Fig. 4. Typical time sequence of the compaction forces and the corresponding vertical displacement movements of the tamper recorded during the compaction of the middle layer of (a) experimental ES08F0, ES09F03 and ES10F05 samples and (b) numerical NS08F0, NS09F03 and NS10F05 samples.

displacement movements of the tamper recorded during the experimental compaction of the middle layer of the unreinforced sand sample (ES08F0) and for both fibre reinforced sand samples (ES09F03 and ES10F05) are shown in Fig. 4a. A very good match between the number of the recorded peak forces like those presented in the figure and the number of tamps counted during the tamping process signifies that one recorded peak force corresponds well to an incremental tamping effort. The displacement recorded by the LVDT includes the movement of the tamper towards the top of the initially deposited soil and this can be omitted as no force is recorded over this distance. Frost and Park (2003) showed that the cumulative compaction effort applied to one layer of soil (plain sand) can be divided into three stages: initial compaction, main compaction, and final compaction. Although these stages are not clearly identifiable from the tests presented here, the compaction of a

layer was complete once the reference collar touched the linear bearing of the Plexiglas plate and no force was subsequently recorded. Before the formation of the following soil layer, it was also checked that the surface of the freshly compacted layer was uniform and levelled. As a general observation, a higher number of tampers and higher peaks are recorded for unreinforced sample (ES08F0) compared with fibre reinforced ones (ES09F03 and ES10F05), Fig. 4a. Fig. 4b presents the equivalent time sequences of the forces as well as imposed vertical displacements during the formation of the middle layer of the numerical samples NS08F0, NS09F03 and NS10F05. In all cases, the reactions are smaller during the first tamping step, while the magnitude of the forces appears to increase with the successive subsequent tamping steps. Once one quarter of the cross-sectional area of the material is compacted, the subsequent tamping requires higher effort as particles encounter higher lateral reactions from the previously compacted section. Although slightly lower forces are recorded once fibres are used and with the increase of fibre content, overall the order of magnitude of the forces for all three samples appears comparable.

5.2. Compaction energy

The compaction energy based on the recorded forces and vertical displacements for all experimental and numerical unreinforced and fibre reinforced samples has been calculated for each layer and for the overall sample formation and the results are presented in Table 4. For comparison purposes, the compaction work is also normalised by the target volume of the layer. Table 4 also shows the averaged values of the energy and normalised energy for all formed experimental samples by layer and overall. The normalised energy required to compact the middle layer appears to be the lowest for the reinforced samples whereas for the unreinforced sand the lowest normalised compaction energy was recorded for the first bottom layer. However, in all cases, the normalised averaged energy is higher for the top layer. By estimating the cumulative force applied to each sand layer, Frost and Park (2003) found that the smallest force was recorded for the second layer of an undercompacted moist tamped sample, while the highest force was given by the compaction of the top layer. Comparing the values of both layer by layer and overall, reinforced sand samples require less compaction energy and the compaction of the loose fibre reinforced sample needs the least energy. The total averaged normalised energy usage for compacting unreinforced soil sample is 21.0 kJ/m^3 while for the fibre reinforced soils with $w_f = 0.3\%$ and $w_f = 0.5\%$, the normalised total compaction energy is 17.5 kJ/m^3 and 13.6 kJ/m^3, respectively. Fig. 5a shows the total averaged normalised energy usage for all the sample densities and fibre contents shown with their standard deviation values.

Concerning the results for the numerically formed samples, with one exception (densest unreinforced sample), the highest normalised compaction energy is recorded for the middle sample layer (Table 4), while the total normalised energy decreases in a similar way as observed for

Table 4
Compaction energy for all experimental and numerical samples generated in this research.

Sample name	Sample No.	Energy [mJ]				Normalised energy [kJ/m^3]			
		layer			Total	layer			Total
		bottom	middle	top		bottom	middle	top	
Experimental investigation									
ES08F0	1	1464.8	3273.6	2735.1	7473.5	19.8	17.0	23.8	19.6
	2	1123.6	3557.4	3103.0	7783.9	15.2	18.5	27.0	20.4
	3	1403.5	3964.9	2139.5	7507.9	18.9	20.6	18.6	19.7
	4	1721.0	3685.2	3101.9	8508.1	23.3	19.2	26.9	22.3
	5	1665.8	3453.5	2985.1	8104.4	22.5	18.0	25.9	21.3
	6	1116.5	4423.8	3342.7	8883.0	15.1	23.0	29.1	23.3
	7	893.67	3992.9	2826.7	7713.3	12.1	20.8	24.6	20.2
	Average	**1175.9**	**3764.5**	**2890.6**	**7996.3**	**18.1**	**19.6**	**25.1**	**21.0**
	St. dev.	**307.4**	**390.3**	**386.3**	**531.8**	**4.1**	**2.0**	**3.4**	**1.4**
ES09F03	1	1185.3	2925.4	1618.4	5729	16.0	15.2	16.2	15.6
	2	1150.4	3519.7	2987.5	7657.6	15.5	18.3	29.9	20.9
	3	1309.5	2454.1	2937.4	6700.9	17.7	12.8	29.4	18.3
	4	1723.6	2207.8	2365.5	6296.9	23.3	11.5	23.6	17.2
	5	1445.8	3223.9	2639.8	7309.5	19.5	16.8	26.4	20.0
	6	1230.8	3291.3	2118.9	6640.9	16.6	17.1	21.2	18.1
	7	1598.2	3238.7	1646.5	6483.4	21.6	16.9	16.5	17.7
	Average	**1266**	**2950**	**2190**	**6405**	**17.12**	**15.36**	**21.9**	**17.5**
	St. dev.	**295.2**	**436.1**	**571**	**788.3**	**4.0**	**2.2**	**5.7**	**2.1**
ES10F05	1	684.76	2230.9	1746.1	4661.7	9.2	11.6	17.5	12.7
	2	1159.8	1364.8	1577.7	4102.3	15.6	7.1	15.8	11.2
	3	538.91	3149.4	1767.7	5456	7.3	16.4	17.7	14.9
	4	1256.9	1529.2	1999	4785.1	17.0	7.9	20.0	13.1
	5	1068.1	2452.9	1544.7	5065.7	14.4	12.7	15.4	13.8
	6	1424	2069.7	1639.8	5133.4	19.2	10.8	16.4	14.0
	7	771.25	3286.8	1639.1	5697.1	10.4	17.1	16.4	15.6
	Average	**986.2**	**2298**	**1702**	**4986**	**13.3**	**12.0**	**17.0**	**13.6**
	St. dev.	**326.3**	**735.4**	**154.1**	**529.3**	**4.4**	**3.8**	**1.5**	**1.4**
Numerical DEM investigation									
NS08F0		219.9	434.9	167.7	**822.6**	0.697	0.530	0.356	**0.511**
NS09F0		64.1	405.4	100.9	**570.4**	0.203	0.495	0.246	**0.369**
NS10F0		49.3	310.3	84.2	**443.8**	0.156	0.378	0.205	**0.287**
NS09F03		63.8	400.3	115.3	**579.4**	0.202	0.489	0.282	**0.375**
NS10F05		55.7	353.4	95.2	**504.3**	0.176	0.431	0.232	**0.326**

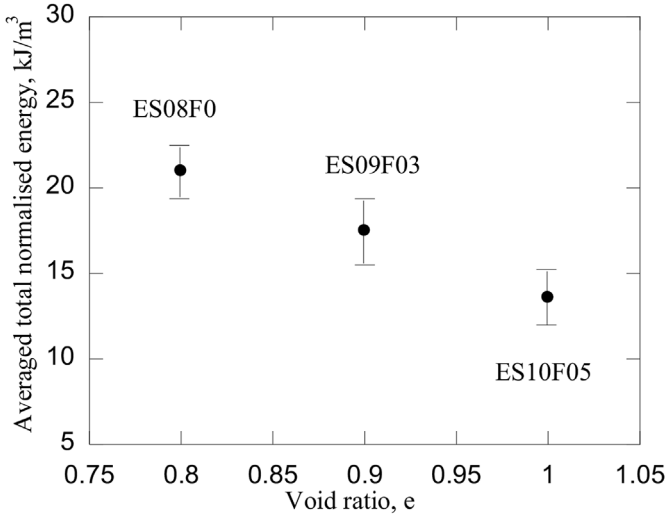

(a)

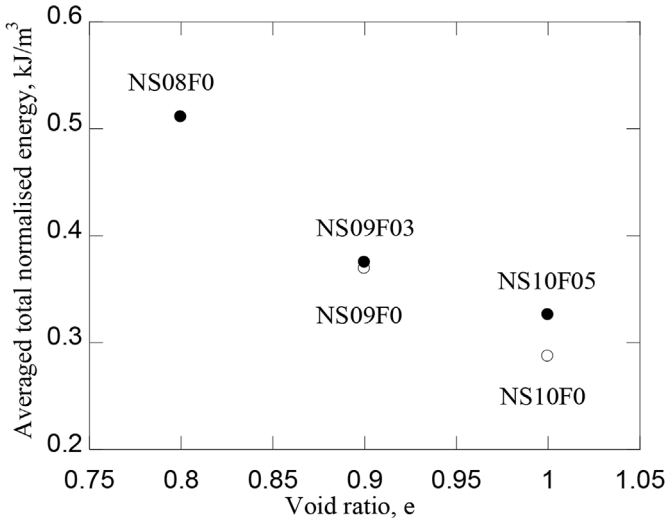

(b)

Fig. 5. Average normalised energy usage for different combinations of densities and fibre contents shown with their standard deviation: (a) experiment; (b) numerical DEM simulation.

the experimental samples (Fig. 5b). For a given sample void ratio, the total normalised compaction energy is higher for the fibre reinforced samples, as expected, considering that fibres show resistance to compaction, but still much lower than the energy required to obtain a denser soil.

5.3. Void ratio distribution

Spatial distributions of the mean void ratio of numerical samples NS08F0, NS09F03 and NS10F05 at the end of formation of each of the three layers are shown in Fig. 6a, b, and c, respectively. Irrespective of the value of the fabrication void ratio, the distribution of the void ratio with the height within each layer varies in a relatively consistent pattern: higher void ratio than the target one at the bottom of the layer, followed by steady reduction with the height (at some level lower than the average void ratio) and then a slight reverse trend closer to the top of the layer, possibly a consequence of the effect of the compaction rigid boundary as demonstrated by Marketos and Bolton (2010). At the bottom of the overlying layer the density is lower (high void ratio) as less compressive force is transmitted to the bottom of the layer located at a further distance from the tamper, as also observed by Frost and Park (2003) and Thomson and Wong (2008). A clear delineation between layers is apparent from the side views of the boundaries between bottom and middle layers of numerically formed unreinforced NS10F0 and fibre reinforced NS10F05 samples in Fig. 7. Relative to the average void ratio value, the increase of the calculated void ratio in the vicinity of the boundaries between the layers is higher for the loose sample and lower for the dense one. However, for one sample density, this increase is much higher at the boundary between the bottom and the middle layer than at the boundary between the middle layer and the top one (Fig. 6). As also observed by Beckett and Augarde (2011), no densification (or over-compaction) of the previously formed layers with the compaction of the top layers is noticeable.

The distributions of the void ratio in the horizontal direction for each one of the numerical samples NS08F0, NS09F03 and NS10F05 and for each successive formed layer are also shown in Fig. 6 (right hand side figures). For all configurations, the density in the central part of the samples appears to be uniform but lower (higher void ratio than the average) at the boundaries, adjacent to the rigid vertical walls. The higher void ratio near the boundaries can be related to a wall type effect on the granular fabric, as previously observed in different experimental and numerical studies (Suzuki et al., 2008; Camenen et al., 2013; Huang et al., 2014; Soriano et al., 2017). For a granular material and a vertical sample wall, the distance from the wall over which the local fabric is affected was estimated to be about 4–5 average particle size diameters (Suzuki et al., 2008). In these simulations, this distance is of the order of 10 mm, which represents about 3 mean size particle diameters. For one sample, the distribution of the void ratio in the horizontal direction does not seem to be affected by the sample layering formation process.

6. Micro-scale observations

6.1. Granular matrix level

Examples of the velocity fields of particles during tamping at the peak of the compaction force as recorded in the numerical simulations are shown in Fig. 8 for three stages: first and second tamping conducted with the one-quarter sample surface tamper and the fifth tamping stage performed with the whole surface rigid plate. Fig. 8a refers to the very loose unreinforced sample, NS10F0, while the effect of the fibres is depicted for the case of the very loose fibre reinforced sample, NS10F05, in Fig. 8b. In these figures, clear blue colour particles signify a stationary state, no movement of the particles. As can be observed, for both samples, the first tamping results in some extensive movement of particles both underneath (over a depth about twice the tamper side-length for the unreinforced sample) and on the lateral side of the tamper, well into the non-directly compacted zones (Beckett and Augarde, 2011). The second tamping stage shows similar patterns, as expected, and some disturbance of the particles in the previously compacted area also occurs. However, in both compaction stages, the volume of the displaced particles (especially the lateral particles) is much more restrained in the fibre reinforced sample than in the unreinforced one. Plate loading tests on fibre reinforced sand by Consoli et al. (2003) and Consoli et al. (2009) showed that the expansion of the sand outside the loading plate area is drastically reduced because of the fibre reinforcement. As a consequence, the inclusion of fibres resulted in a radical change in the failure mechanisms compared with the unreinforced soil. Concerning the final tamping stage, again, at the peak of the compaction force, the particles near the rigid plate of the reinforced sample are more affected than the bottom half when compared with the unreinforced sample.

These observations can also be corroborated with the corresponding developed force chains in the matrix particles (Fig. 9). The force

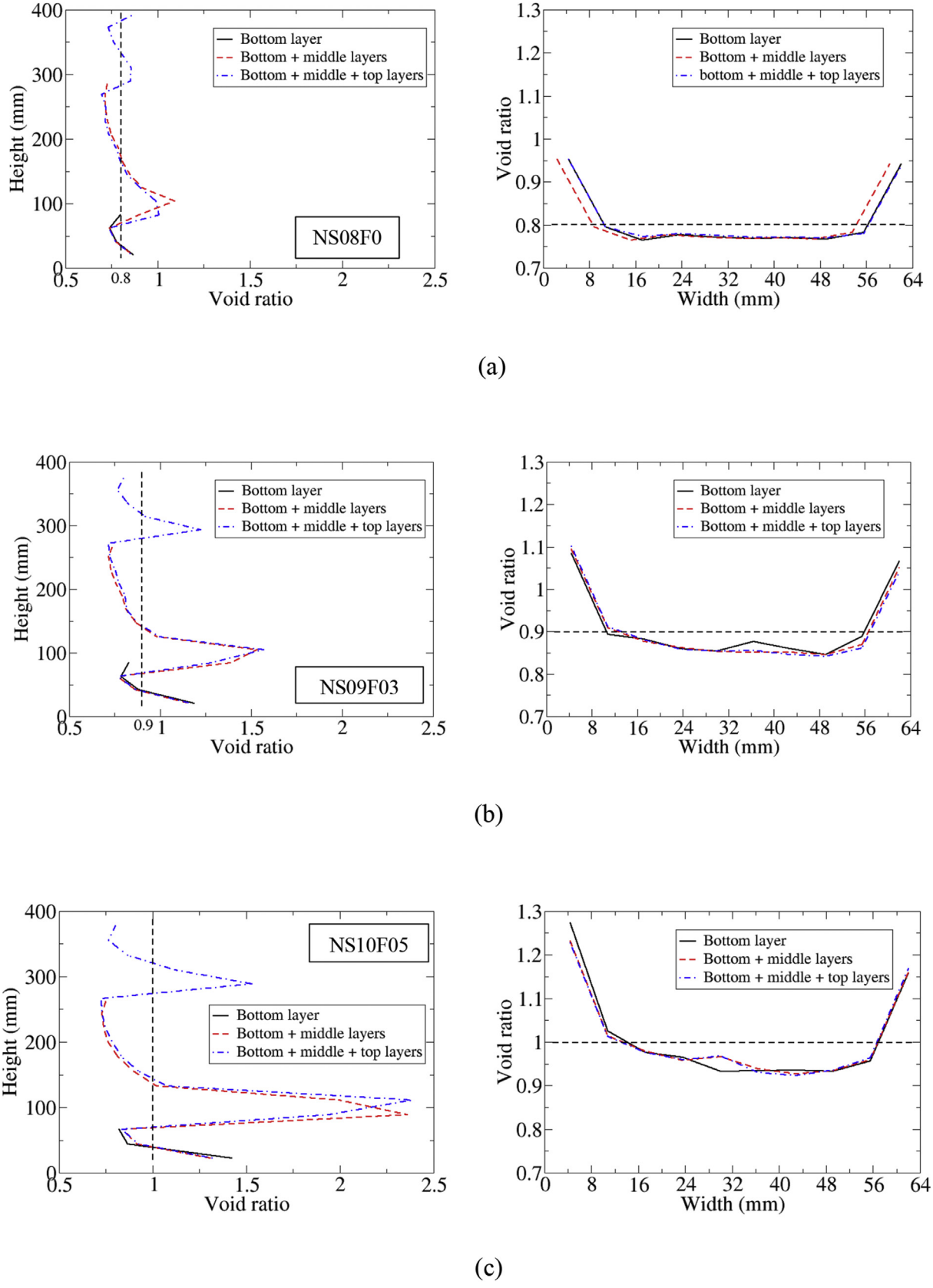

Fig. 6. Computed distribution of void ratio over the height (left) and in the horizontal direction (right) at the end of first layer formation, end of second layer formation and end of sample formation for (a) NS08F0; (b) NS09F03; (c) NS10F05 numerical samples.

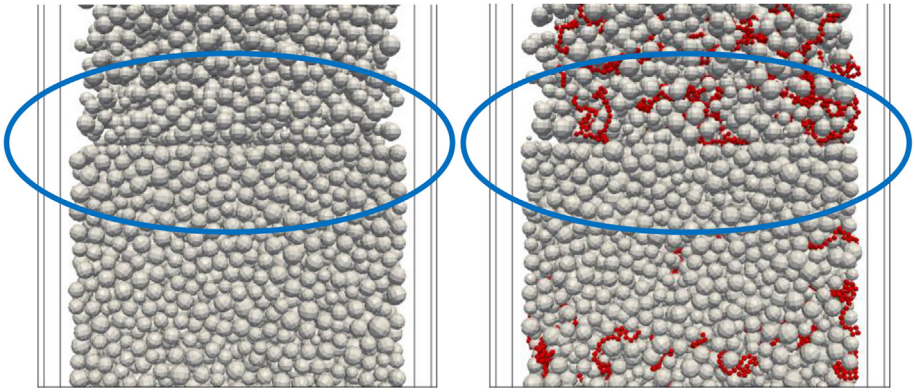

Fig. 7. Detail of the boundary between the first layer and the second layer for two numerical DEM samples: unreinforced sample (left) and fibre reinforced sample (right).

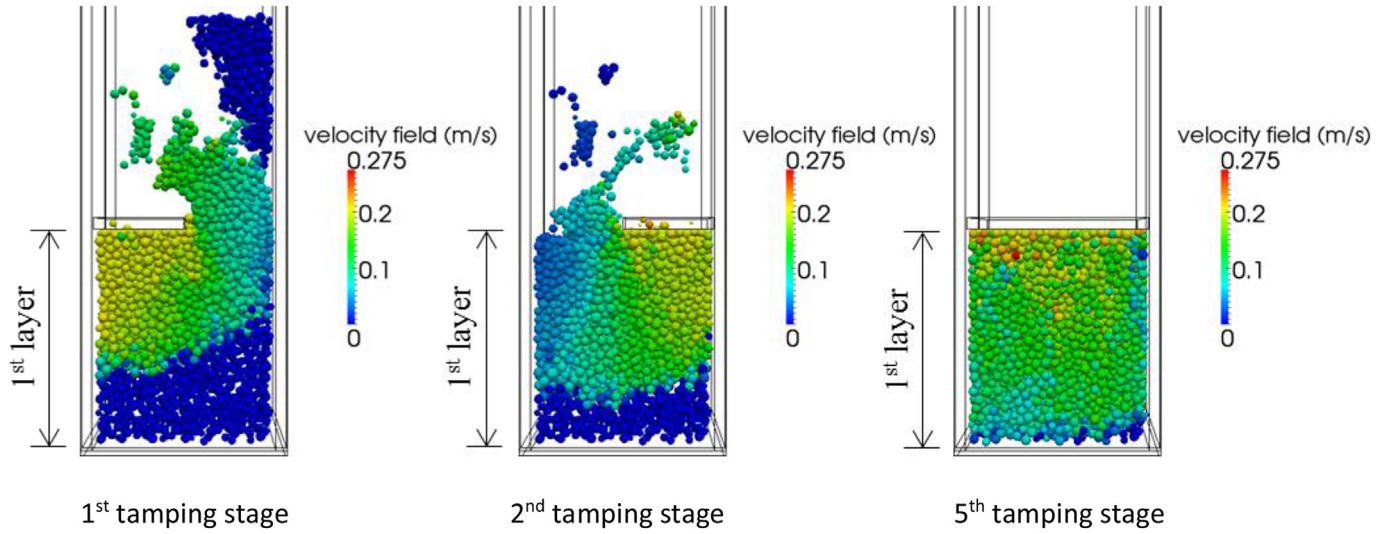

Fig. 8. Velocity field at peak compressive stress during 1st, 2nd and 5th tamping stages for: (a) unreinforced NS10F0 and (b) reinforced NS10F05 samples.

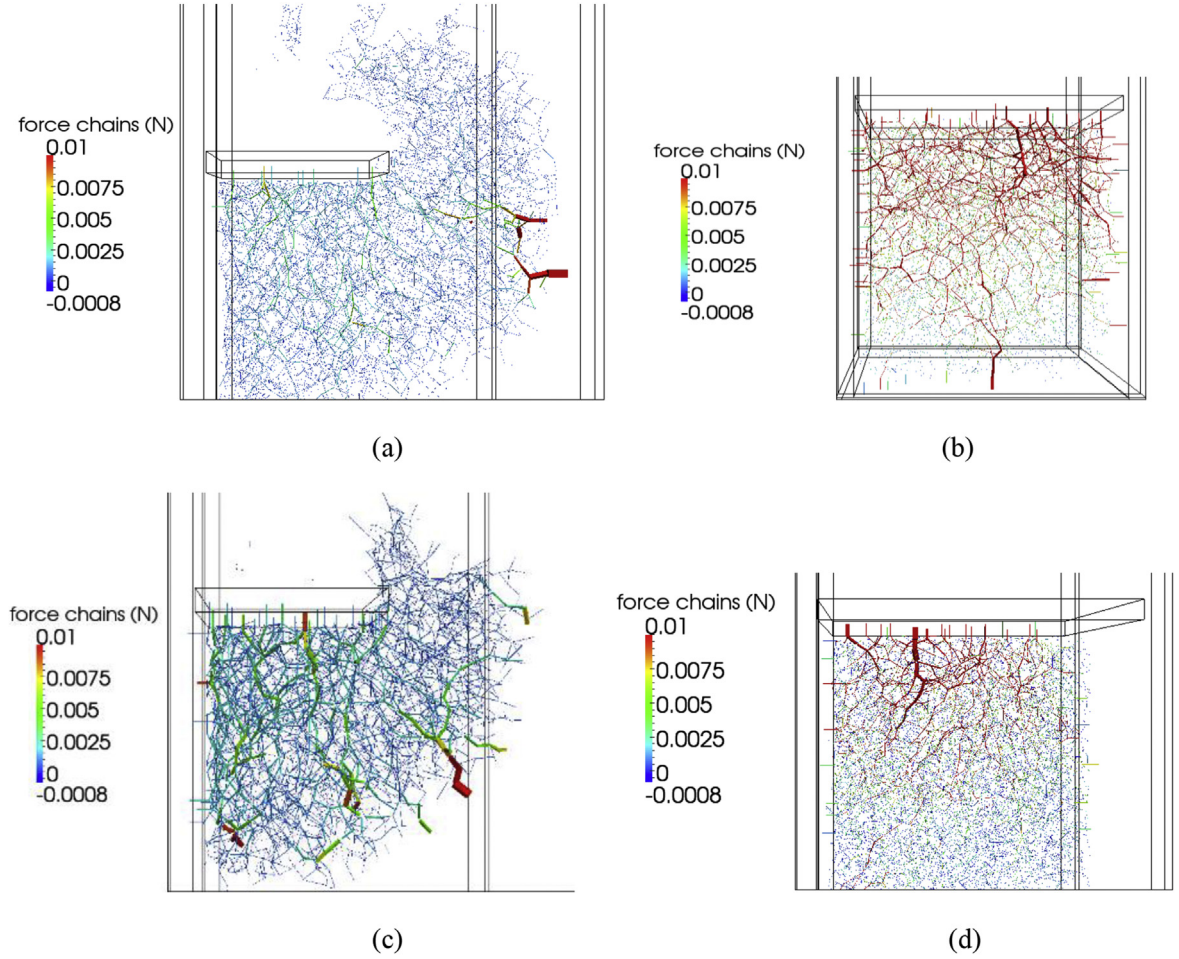

Fig. 9. Development of the chain of forces at the peak of the compressive stress in: (a) NS10F0, 1st tamping stage; (b) NS10F0, 5th tamping stage; (c) NS10F05, 1st tamping stage, and (d) NS10F05, 5th tamping stage.

particle chains for the initial (first) and final (fifth) tamping stages of the unreinforced sample NS10F0 (Fig. 9a and b, respectively) show a denser and finer network than for the equivalent tamping stages of the reinforced sample NS10F05 (Fig. 9c and d). The extent of the force chain network is much more restrained and localised to the tamping device for the fibre reinforced sample. The reaction forces developed during tamping are higher and higher energy is required to compact the reinforced material.

6.2. Fibre level

For each numerically formed fibre reinforced samples, the averaged tensile stress computed for all the bond contacts within the fibres developed during all the successive five tamping stages for each layer - bottom, middle and top - are plotted in Fig. 10. Fig. 10a presents the mobilised stress in the fibres for NS09F03, while Fig. 10b shows the variation of the average stress for the NS10F05 sample. The vertical dash lines demarcate the successive tamping stages. As a sign convention, a positive sign of the stress denotes a tensile stress, and as can be observed mainly tensile stresses are developed in the fibres during the layers' formation. The effect of the fibre content cannot be clearly isolated from comparison between both Fig. 10a and b as the densities of the granular matrix are not the same for these samples. However, while the trends of the average fibre stresses for each layer seem to be consistent for both samples, the magnitude of the mobilised stresses in the fibres are lower for the NS10F05 sample which has more fibres and fewer granular particles. For the bottom layers, the evolution of the fibre stress in each tamping stage shows a dense succession of peaks and troughs, with no clear patterns for the timing of occurrence of the maximum peak values. An interesting observation can be made for the middle-compacted layer: for both samples, in the first stage of the compaction while the soil reaction is negligible (see Fig. 4), the average fibre stress remains constant. Once the compaction advances, the mobilised fibre stress first decreases (as consequence of the particle rearrangements and heave of previously compacted material), and then increases up to the end of the tamping stage. The level of the average stress increases with the tamping stages, while the maximum stress is always recorded in the fifth (and final) stage towards the end of the tamping. These maxima seem identical for both samples, but overall the mobilised fibre tensile stress is clearly smaller in the very loose sample with a higher number of fibres too. Consoli et al. (2005) showed that the fibres are in tension even when the sample is undergoing compressive volumetric strains induced by isotropic compression loading. Similar observations can be made for the mobilised average fibre stresses during the formation of the final layer. However, occasionally the average fibre stress shows some compressive excursions, and this can physically occur due to local particle fabric re-arrangements, as also shown by Ibraim et al. (2006).

6.3. Fabric of matrix and fibre orientation distribution

Fig. 11a shows the 2D polar histogram representations of the distributions of the normal contacts for all the matrix particles of all the numerical samples over horizontal X-Y and vertical X-Z planes at the end of the sample formation. The rose diagrams describing the angular distribution of the particle normal contacts in the horizontal plane are

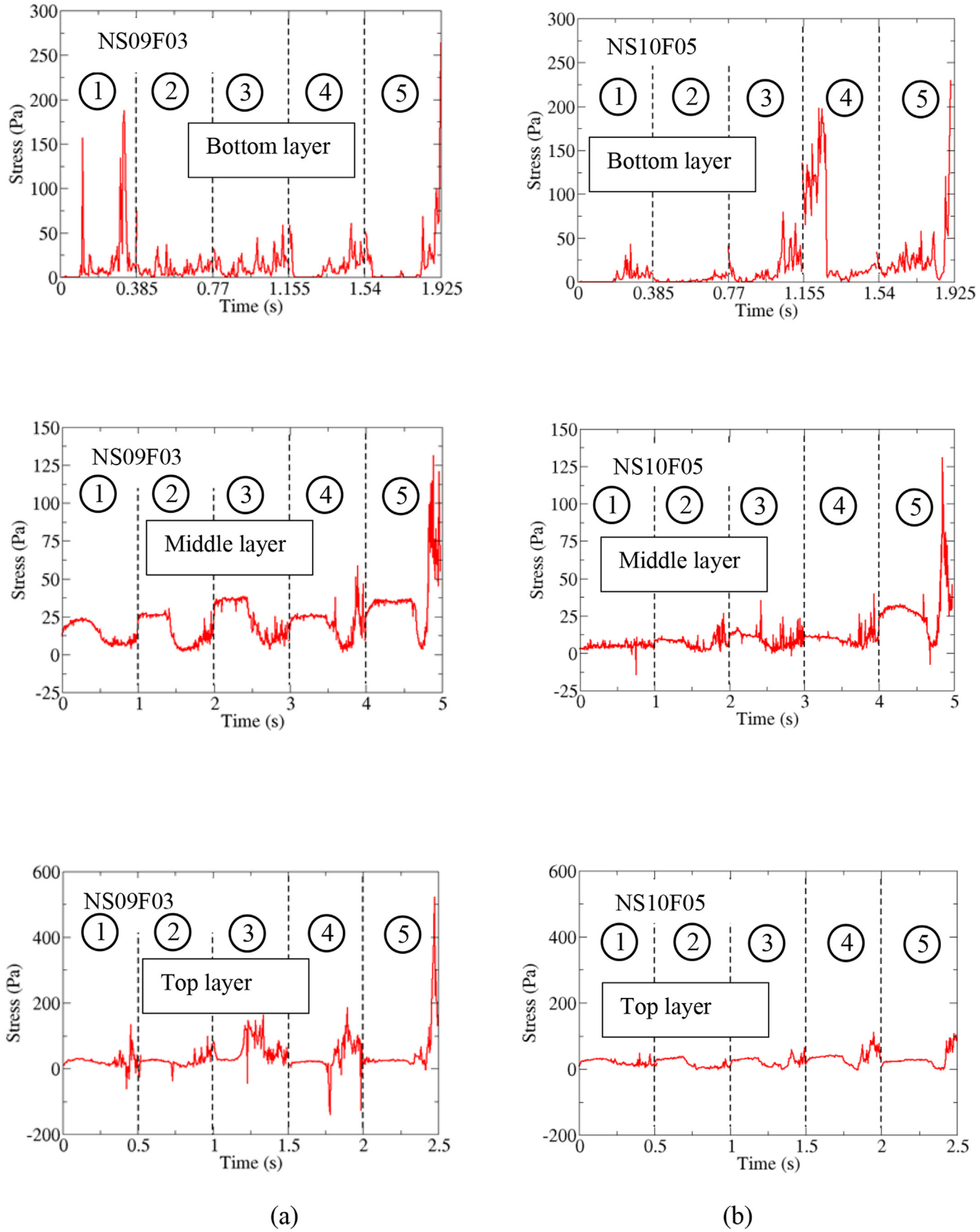

Fig. 10. Average stress mobilised in the fibres during the five successive tamping stages for each layer of the numerical samples: (a) NS09F03 and (b) NS10F05. horizontal X-Y plane vertical X-Z plane.

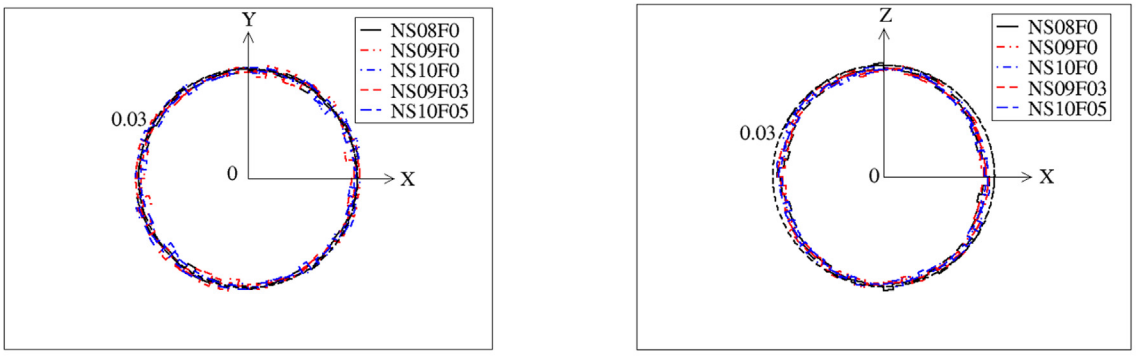

(a)

horizontal X-Y plane vertical X-Z plane

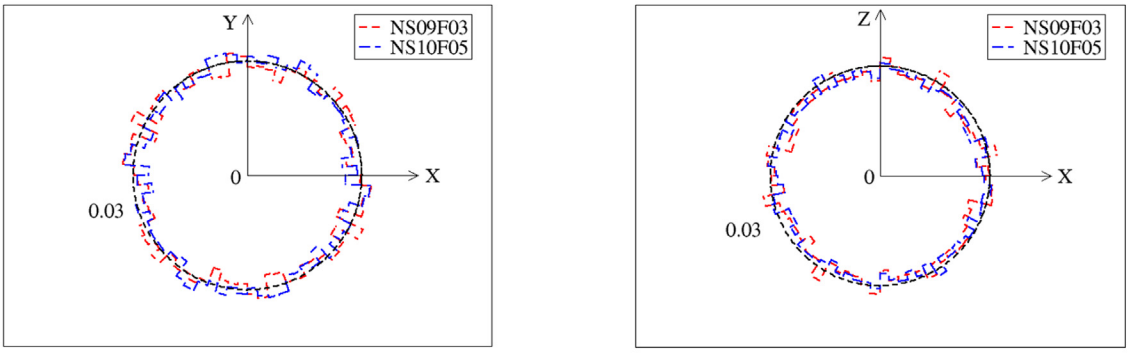

(b)

horizontal X-Y plane vertical X-Z plane

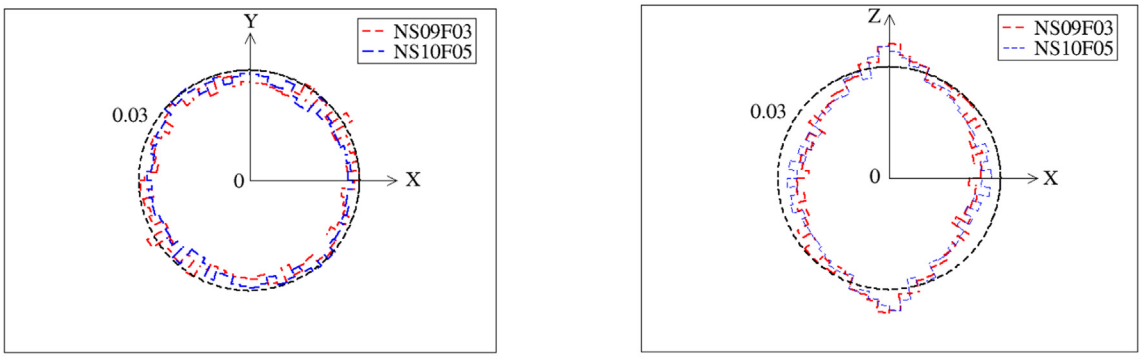

(c)

Fig. 11. (a) Distribution of the particle normal contacts with respect to the horizontal (X–Y) and vertical (Z–X) planes for the matrix of all fibre reinforced and unreinforced numerical fully formed samples; (b) and (c) distribution of the particle normal contacts with respect to the horizontal (X–Y) and vertical (Z–X) planes for the particles forming the fibres in all three sample layers: (b) before compaction and (c) after compaction. Figures (b) and (c) provide the distribution of fibre orientations.

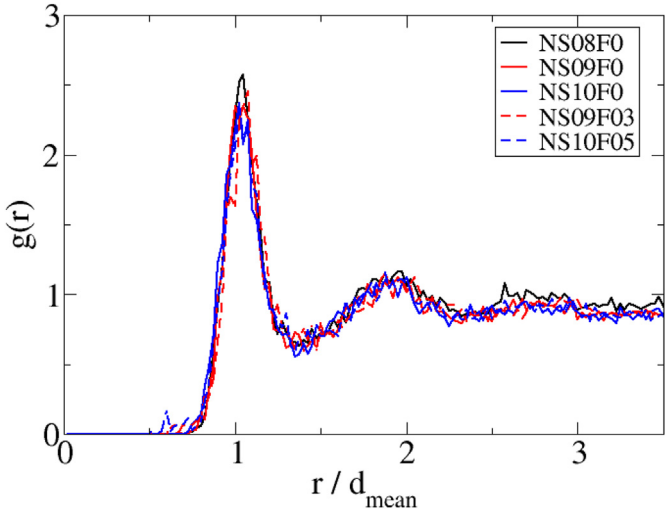

Fig. 12. Pair correlation function *g(r)* (equation (1)) computed for the matrix in the whole formed numerical samples (all five fibre reinforced and unreinforced samples).

perfectly symmetric about the vertical Z-axis, as expected for an axi-symmetry fabric property. A slight anisotropy, induced by the vertical tamping process of the distribution of the contact orientations, is visible in the Z direction, and this is perfectly consistent for all the samples, whether very loose of dense, as well as unreinforced or fibre reinforced.

The structure of a granular system can be examined using the radial distribution function, *g(r)*, which gives the possibility of identifying the formation of ordered packing, as proposed by Silbert et al. (2002):

$$g(r) = \frac{dn/[N(N-1)]}{V/4r^2dr} \quad (1)$$

where N and V are the number of particles and total volume of the sample, respectively, and dn is the number of pairs of particle centres situated at a distance between r and $r + dr$. Fig. 12 shows the variation of the radial distribution function for the matrix phase and for all the numerically formed samples. For all the sample configurations, and independent of their densities and fibre content, the correlations are clearly centred on the mean particle diameter, d_{mean}, while the attenuation of the amplitude from this peak indicates no ordered packing detection.

The study of the normal contacts between the particles forming the fibres provides an indication of the distribution of the fibre orientation throughout the fibre reinforced samples. Fig. 11b shows the 2D polar histogram representations of the distributions of the normal contacts for all the fibres of the numerical samples over the horizontal X-Y and vertical X-Z planes before compaction and formation of the layers, while Fig. 11c presents the distributions of the normal over the same planes at the end of the sample formation. Before compaction, the distributions of the fibre orientation are random and symmetric in both the X-Y and vertical X-Z planes (Fig. 11b). This symmetry is conserved in X-Y plane following the sample formation. However, a slight anisotropy of orientations (independent of fibre content and sample density) seems to occur with the sample formation process, with a vertical alignment of the fibres. This seems in contradiction with the conclusions of the studies of fibre orientation distribution resulted from fabrication like moist tamping on laboratory samples by Diambra et al. (2007) and Ibraim et al. (2012), which show a rather sub-horizontal fibre orientation distribution. However, it must be emphasised that the formation of the numerical samples does not include the mixing and deposition stages as in the experimental studies. Therefore these results seem to suggest that in practice both the mixing and mixture deposition phases are controlling the fibre orientation distribution and not the way in which the final compaction of the mixture stage is conducted. Ibraim et al. (2012) and Soriano et al. (2017) showed that the fibre orientation distributions of fibre reinforced laboratory samples resulting from two different fabrication methods, moist tamping and vibration of the entire material, are similar. In both fabrication methods, the mixing and mixture deposition phases were identical.

7. Conclusion

This paper has investigated the aspects related to the energy required for the compaction phase of unreinforced and fibre reinforced samples formed in laboratory. The experimental determination of the energy required for the compaction stage of sample fabrication has been complemented by numerical DEM simulations of compacted counterpart analogue granular samples to gain further insight into the response to tamping and sample formation of both individual granular matrix and fibre phases. The research study has led to the following conclusions:

- Although fibres show resistance to compaction, and for a given mass of dry sand and a given sample volume more compaction energy would be necessary for the construction of samples with higher fibre contents, in practice it may appear more appropriate to replace a dense sand with a less dense one but reinforced with fibres. The assessment of the compaction energy required to construct three different samples with similar strength properties - one medium dense unreinforced and two, loose and very loose, reinforced with 0.3% and 0.5% of fibres, respectively - showed that the normalised energy decreases with the decrease in density and increase in fibre content. In these conditions, for the construction of real scale geotechnical systems, soil strengthening using fibres as opposed to soil densification may require less compaction energy.
- The results from the parallel numerical DEM study of unreinforced and fibre reinforced analogue granular samples corroborate well the experimental findings on the energy consumption during compaction stages, showing similar tendencies. In addition, it was shown that for a given granular density, more energy is required when fibres are added.
- As observed by other studies, the distribution of the density within individual layers and from one layer to another induced by moist tamping is not uniform. Effects of the vertical sample wall and compaction device on the density were observed on the numerical simulations.
- Results of DEM simulations suggest that the presence of fibres reduces the volume of displaced particles during each tamping stage, while the particle force contact network is much more restrained and localised at the tamping device interface. The density of the particle force chains is lower for the reinforced samples than the unreinforced one.
- DEM simulations reveal that during tamping process, the fibres are mobilised in tension. The tensile stresses in fibres vary during the tamping stage and larger tensile stresses are mobilised at the end of the compaction stage.
- The angular distribution of the matrix particle normal contacts does not seem to be affected by the presence of fibres compared with unreinforced material and no ordered packing formation was detected on both unreinforced and fibre reinforced sample. The distribution of the fibre orientation assessed from the numerical simulations and its comparison with previous experimental results appear to suggest that the fibre orientation is mainly controlled by the mixing and deposition phases of the mixtures rather than the formation stage (compaction or vibration).

While this research retains a fundamental nature, the extrapolation of the results and conclusions to the real scale of geotechnical systems would require further and specific research.

Acknowledgment

The authors gratefully acknowledge the financial support provided by the UK Royal Academy of Engineering under the Newton Research Collaboration Programme (Grant reference: NRCP1415/2/2). Part of this work was also possible with the support of University of Bristol and by the UK Engineering and Physical Sciences Research Council (Grants EP/J010022/1 and EP/G064180; data necessary to support the conclusions are included in the paper).

References

Beckett, C.T., Augarde, C.E., 2011. A novel image-capturing technique for the experimental study of soil deformations during compaction. Geotech. Test J. 34 (6), 571–578.

Cambou, B., Jean, M., Radjai, F., 2010. Micromechanics of Granular Materials. ISTE, London.

Camenen, J.F., Descantes, Y., 2017. Geometrical properties of rigid frictionless granular packings as a function of particle size and shape. Phys. Rev. 96, 012904.

Camenen, J.F., Descantes, Y., Richard, P., 2012. Effect of confinement on dense packings of rigid frictionless spheres and polyhedra. Phys. Rev. 86, 061317. http://dx.doi.org/10.1103/PhysRevE.86.061317.

Camenen, J.F., Cavaretta, I., Hamlin, S., Ibraim, E., 2013. Experimental and numerical assessment of a cubical sample produced by pluviation. Géotech. Lett. 3 (2), 44–51. http://dx.doi.org/10.1680/geolett.13.00028.

Cavarretta, I., Rocchi, I., Coop, M.R., 2011. A new interparticle friction apparatus for granular materials. Can. Geotech. J. 48 (12), 1829–1840.

Consoli, N.C., Vendruscolo, M.A., Prietto, D.M.P., 2003. Behavior of plate load tests on soil layers improved with cement and fiber. J. Geotech. Geoenviron. Eng. 129 (1), 96–101.

Consoli, N.C., Dal Toe Casagrande, M., Coop, M.R., 2005. Effect of fibre reinforcement on the isotropic compression behaviour of a sand. J. Geotech. Geoenviron. Eng. 131 (11), 1434–1436.

Consoli, N.C., Casagrande, M.D.T., Thomé, A., Rosa, F.D., Fahey, M., 2009. Effect of relative density on plate loading tests on fibre-reinforced sand. Geotechnique 59 (5), 471.

Diambra, A., Ibraim, E., 2014. Modelling of fibre–cohesive soil mixtures. Acta Geotechnica 9 (6), 1029–1043.

Diambra, A., Ibraim, E., 2015. Fibre-reinforced sand: interaction at the fibre and grain scale. Geotechnique 65 (4), 296–308.

Diambra, A., Russell, A.R., Ibraim, E., Muir Wood, D., 2007. Determination of fibre orientation distribution in reinforced sand. Geotechnique 57 (7), 623–628. http://dx.doi.org/10.1680/geot.2007.57.7.623.

Diambra, A., Ibraim, E., Muir Wood, D., Russell, A.R., 2010. Fibre reinforced sands: experiments and modelling. Geotext. Geomembranes 28, 238–250.

Diambra, A., Ibraim, E., Muir Wood, D., Russell, A.R., 2011. Modelling the undrained response of fibre reinforced sand. Soils Found. 51 (4), 625–636.

Dubois, F., Jean, M., 2003. LMGC90: une Platforme de Development Dedie a la Modelisation des Problemes d'Interaction. In: Actes du sixieme colloque national en calcul des structures CSMA-AFM-LMS 1. pp. 111–118.

Eliadorani, A., Vaid, Y.P., 2003. Discussion of 'Effect of undrained creep on instability of loose sand'. Can. Geotech. J. 40, 1056–1057.

Flavigny, E., Desrues, J., Balayer, B., 1990. Note technique: le sable d'Hostun R.F. Rev. Fr. Geotech. 53, 67–70.

Frost, J.D., Park, J.-Y., 2003. A critical assessment of the moist tamping technique. Geotech. Test J. 26 (1), 57–70.

Gray, D.H., Ohashi, H., 1983. Mechanics of fiber reinforcement in sands. J. Geotech. Eng., ASCE 109 (3), 335–353.

Hoare, D.J., 1979. Laboratory study of granular soils reinforced with randomly oriented discrete fibers. In: Proc. Of the Int. Conference on Soil Reinforcement, Paris, vol. 1. pp. 47–52.

Horn, H.M., Deere, D.U., 1962. Frictional characteristics of minerals. Geotechnique 12 (4), 319–335.

Huang, X., Hanley, K.J., O'Sullivan, C., Kwok, F.C.Y., 2014. Effect of sample size on the response of DEM samples with a realistic grading. Particuology 15 (August), 107–115.

Ibraim, E., Fourmont, S., 2007. Behaviour of sand reinforced with fibres. In: Soil Stress-strain Behavior: Measurement, Modeling and Analysis, vol. 146. pp. 807–818. http://dx.doi.org/10.1007/978-1-4020-6146-2_60.

Ibraim, E., Muir Wood, D., Maeda, K., Hirabashi, H., 2006. Fiber-reinforced granular soils behavior. In: Hyodo, E.M., Murata, H., Nakata, Y. (Eds.), Proc. Int. Symp. Geomechanics and Geotechnics of Particulate Media, Ube, Yamaguchi, Japan. Taylor & Francis Group, pp. 443–448.

Ibraim, E., Diambra, A., Muir Wood, D., Russell, A.R., 2010. Static liquefaction of fibre reinforced sand under monotonic loading. Geotext. Geomembranes 28, 374–385.

Ibraim, E., Diambra, A., Russell, A.R., Wood, D.M., 2012. Assessment of laboratory sample preparation for fibre reinforced sands. Geotext. Geomembranes 34, 69–79.

Jean, M., Moreau, J.-J., 1992. In: In: Curnier, A. (Ed.), Contact Mechanics, vols. 31–48 (Lausanne).

Ladd, R.S., 1978. Preparing specimens using undercompaction. Geotech. Test J. 1 (1), 16–23.

Laniel, L., Alart, P., Pagano, S., 2008. Discrete element investigations of wire-reinforced geomaterial in a three-dimensional modeling. Comput. Mech. 42, 67–76.

Lings, M.L., Dietz, M.S., 2005. The peak strength of sand-steel interfaces and the role of dilation. Soils Found. 45 (6), 1–14.

Maeda, K., Ibraim, E., 2008. DEM analysis of 2D fibre-reinforced granular soils. In: Proc. Int. Symp. Deformation Characteristic of Geomaterials, IS-Atlanta, vol. 2. pp. 623–628.

Marketos, G., Bolton, M.D., 2010. Flat boundaries and their effect on sand testing. Int. J. Numer. Anal. Meth. GeoMech. 34, 821–837.

Michalowski, R.L., Čermák, J., 2003. Triaxial compression of sand reinforced with fibers. J. Geotech. Geoenviron. Eng. 129 (2), 125–136.

Mitarai, N., Nori, F., 2006. Wet granular materials. Adv. Phys. J. 55 (1–2), 1–45.

Moreau, J.J., 1994. Some numerical methods in multibody dynamics: application to granular materials. European J. Mech. A 13, 93–114.

Muir Wood, D., Diambra, A., Ibraim, E., 2016. Fibres and soils: a route towards modelling of root-soil systems. Soils Found. 56 (5), 765–778.

Murray, J.J., Frost, J.D., Wang, Y., 2000. Behaviour of s sandy silt reinforced with discontinuous recycled fibre inclusions. Transport. Res. Rec. 1714, 9–17.

Rowe, P.W., 1962. The stress–dilatancy relation for static equilibrium of an assembly of particles in contact. In: Proc. R. Soc. A, vol. 269. pp. 500–527.

Saint-Cyr, B., Radjaï, F., Delenne, J.-Y., Sornay, P., 2013. Cohesive granular materials composed of nonconvex particles. Phys. Rev. 87, 052207.

Senetakis, K., Coop, M.R., Todisco, C., 2013. The inter-particle coefficient of friction at the contacts of Leighton Buzzard sand quartz minerals. Soils Found. 53 (5), 746–755.

Silbert, L.E., Ertas, D., Grest, G.S., Halsey, T.C., Levine, D., 2002. Geometry in frictionless and friction sphere packings. Phys. Rev. E 65, 031304.

Soriano, I., Ibraim, E., Andò, E., Diambra, A., Laurencin, T., Moro, P., Viggiani, G., 2017. 3D fibre architecture of fibre-reinforced sand. Granul. Matter 19, 75. https://doi.org/10.1007/s10035-017-0760-3.

Soulié, F., Cherblanc, F., El Youssoufi, M.S., Saix, C., 2006. Influence of liquid bridges on the mechanical behaviour of polydisperse granular materials. Int. J. Numer. Anal. Meth. GeoMech. 30 (3), 213–228.

Suzuki, M., Shinmura, T., Iimura, K., Hirota, M., 2008. Study of the wall effect on particle packing structure using x-ray micro computed tomography. Adv. Powder Technol. 19 (2), 183–195.

Taboada, A., Chang, K.-J., Radjaï, F., Bouchette, F., 2005. Rheology, force transmission, and shear instabilities in frictional granular media from biaxial numerical tests using the contact dynamics method. J. Geophys. Res. 110, 1–24.

Thomson, P.R., Wong, R.C.K., 2008. Specimen nonuniformities in water-pluviated and moist-tamped sands under undrained triaxial compression and extension. Can. Geotech. J. 45 (7), 939–956.

Vaid, Y.P., Sivathayalan, S., Stedman, D., 1999. Influence of specimen-reconstituting method on the undrained response of sand. Geotech. Test J. 22 (3), 187–195.